Frequency bandgap enhancement in locally resonant metasurfaces for $S0$ Lamb wave mode using topology-optimized resonators

L. S. S. Pillarisetti,[1] D. Giraldo Guzman,[2] J. Keirn[1], S. Sridhar,[1] C. Lissenden,[1] M. Frecker,[2] and P. Shokouhi[1,a)]

[1] *Department of Engineering Science and Mechanics, The Pennsylvania State University, University Park, PA 16802*

[2] *Department of Mechanical Engineering, The Pennsylvania State University, University Park, PA 16802*

Elastodynamic metasurfaces composed of surface-mounted resonators show great promise for guided wave control in diverse applications, e.g., seismic and vibration isolation, nondestructive evaluation, or surface acoustic wave devices. In this work, we revisit the well-studied problem of “rod-shaped” resonators coupled to a plate to reveal the relationship between the resonator’s resonances and antiresonances obtained under unidirectional harmonic excitation and the resultant frequency bandgap for S_0 Lamb mode propagation once a metasurface is arranged. This relationship is shown to hold true even for non-prismatic resonators, such as those presented in our recent studies, in which we established a systematic resonator design methodology using topology optimization by matching a single resonator's antiresonance with a predefined target frequency. Our present study suggests that considering the waveguide (plate) during the resonator design is not essential and encourages a feasible resonator-design approach to achieve wide bandgaps just by customizing a single resonator’s resonances and antiresonances. We present a topology optimization design methodology for resonators that drive resonances away from antiresonances, i.e., a resonance gap enhancement, yielding a broadband S_0 mode bandgap while ensuring the desired bandgap formation by matching antiresonances with a target frequency. The transmission loss of metasurfaces composed with topology-optimized resonators is numerically verified, confirming the generation of wider bandgaps compared to resonators designed without resonance gap enhancement and broadening the applicability of locally resonant metasurfaces.

I. INTRODUCTION

While metamaterials are defined broadly across disciplines from optics to acoustics, elastodynamic metamaterials are an emergent subcategory of engineered, dynamic structures to control elastic waves [1]. These metamaterials typically utilize one of two mechanisms for wave control: Bragg scattering and local resonance. The former is the basis for phononic crystals, which are composites with periodic structures that scatter and attenuate waves with wavelengths comparable to their lattice constant [2], [3]. Alternatively, locally resonant metamaterials generate bandgaps by achieving unusual properties of negative effective mass density and elastic modulus due to the local resonance phenomenon that arises from the hybridization of a propagating wave with the embedded resonant inclusions [4], [5]. The local resonance approach is often preferred for elastic wave control as it facilitates employing subwavelength-spaced resonant structures, and it does not require lattice periodicity. While there has been a lot of research employing local resonance to generate bandgaps for elastic wave control, there has been an increased attention in recent years to widening bandgaps such that they span across broad frequency ranges.

Graded metasurfaces are used to achieve wider bandgaps through the "rainbow effect" by systematically tuning the resonance frequencies of resonators comprising the metasurface [6]–[10]. Alternatively, the Topology Optimization (TO) method, widely used in solving problems across structural mechanics, acoustics, optics, and electromagnetics, has drawn attention in tailoring bandgaps for phononic crystals and metasurfaces [11]–[15]. Most of these studies share a common design

a) Correspondence should be addressed to parisa@psu.edu

objective, i.e., maximize bandgaps from dispersion analyses considering the unit cell consisting of a resonator mounted on a portion of the waveguide [16], [17] or by modifying the waveguide's topology to induce frequency bandgaps [13], [18]. Although only a few publications have directly addressed the topological design of individual resonators, they have employed 2D simplifications and low-refinement meshes to enable the use of genetic algorithms [17], [19]–[21]. The TO design of a metasurface relying on computationally expensive dispersion analyses, also requires the identification of an opening bandgap at a desired or random frequency range and the selection of lower and upper bandgap bounds at the appropriate wavenumber values where the wave speed approaches zero. For gradient-based TO, a complex derivation of analytical sensitivity function considering Bloch-Floquet periodic conditions would be necessary. For non-gradient based TO, the optimization problem must be simplified so that the computational solution is feasible. An efficient and rational design methodology for three-dimensional local resonators capable of generating wide frequency bandgaps is lacking.

In this paper, instead of dealing with this complex design problem, we propose the systematic design of local resonators by isolating them from the waveguide and replacing the resonator-waveguide interaction with unidirectional harmonic loads that mimic the propagating wave mode forcing. The resonator's dynamic response to these unidirectional harmonic loads, i.e., resonances and antiresonances, is then manipulated so that frequency bandgaps open around an antiresonance frequency while the surrounding resonances are pushed apart to maximize the bandgap width. Such topology-optimized resonators whose design process does not rely on considering the waveguide-resonator interactions but instead on the underlying wave physics, offer significant advantages in reducing computational complexity. This approach is particularly useful for lower frequency and surface wave control applications, where the waveguide is a half-space that requires a fine finite element mesh during the computation.

Designing local resonators by tailoring their dynamic response requires a comprehensive understanding of how their resonances and antiresonances shape the resultant frequency bandgap for a desired guided mode, e.g., S_0 or A_0 Lamb wave modes; understanding the local resonance mechanism is the key to generating bandgaps for metasurfaces. The role of longitudinal resonances and antiresonances of rod resonators in generating bandgaps for the A_0 Lamb wave in a plate was demonstrated experimentally and analytically for the first time in the pioneering works of Rupin *et al.* [22] and Williams *et al.* [23]. Longitudinal resonances and antiresonances are the frequencies at which the maximum and minimum out-of-plane displacement response is attained at the application point of harmonic excitations during longitudinal vibrations. Similarly, flexural resonances and antiresonances correspond to the frequencies of maximum and minimum in-plane displacement response due to flexural vibration modes. Ignoring the S_0 mode and the rod's flexural resonances, Williams et al. demonstrated that the start and end of an A_0 mode bandgap coincide, respectively, with the rod resonator's longitudinal antiresonance and resonances [23]. This is in contrast to that observed for surface waves, where resonance frequencies determine the bandgap start while antiresonance frequencies are positioned at the bandgap end [24]–[26]. Colquitt et al. [27] extended the analytical model of Williams by studying the interaction of both longitudinal and flexural vibrations with the A_0 and S_0 modes. Similar to surface waves, the A_0 mode was demonstrated to hybridize with both longitudinal and flexural resonances, whereas the S_0 mode only hybridizes with flexural resonances, resulting in the corresponding bandgaps for both modes. Constraining the out-of-plane displacement component on the plate's surface - representing the longitudinal antiresonance of the resonator - was the key to suppressing the A_0 mode [23], as it was later confirmed by Lissenden et al. [28] who imposed a set of BCs to inhibit A_0 mode propagation, i.e., Mindlin BCs. In contrast to the A_0 mode, clamping the in-plane displacement on the plate's surface - representing the flexural antiresonance of the resonator - i.e., applying Auld BCs, is the necessary condition to achieve S_0 mode suppression [28], [29]. Building on this observation, Guzman et al. [30] proposed a density-based topology optimization approach for designing metasurfaces to obtain S_0 mode suppression by matching their resonators' flexural antiresonances with a target bandgap frequency, however, the resulting bandgaps are narrow mainly due to the high Q-factor of flexural resonances. This highlights the need for new strategies to obtain wide bandgaps.

The primary goal of this study is to design metasurfaces to inhibit S_0 Lamb wave mode propagation over a wide frequency range by considering the guided mode propagation characteristics, the local resonators' properties, and the target bandgap frequency without relying on parametric tuning of dispersion curves. To assess the feasibility of excluding waveguide considerations in resonator design, we present an analysis of (i) how the resonator's resonances and antiresonances under in-plane harmonic excitation, mimicking the S_0 mode wave structure, relate to the resonator response observed under S_0 mode propagation, and (ii) what is their relation to the bandgap bounds after a metasurface has been constituted. While the influence of resonances and antiresonances in forming bandgaps for rod-shaped resonators has been examined for the A_0 Lamb wave mode [23] and surface waves [24]–[26], this study focuses on the S_0 mode, which has not been explored in similar context. We therefore revisit the problem of rod-shaped resonators mounted on a plate, demonstrating a strong connection among their resonances, antiresonances, and the obtained frequency bandgap. This connection motivates a topology optimization-based resonator design approach to enhance bandgaps by tailoring these critical frequencies. We further demonstrate numerically and experimentally that these relations are preserved even for non-prismatic topology-optimized resonators designed for S_0 mode suppression by tailoring a single antiresonance frequency [30]. Our study demonstrates the feasibility of a resonator design that yields wide S_0 bandgaps by forcing the resonator's resonances away from the antiresonances under in-plane harmonic excitation. We validate the efficacy of topology-optimized resonators using frequency-domain finite element simulations, revealing wider bandgaps compared to those for the metasurfaces without bandgap enhancement.

The remainder of the paper is arranged as follows. Section II reviews the relations among resonances, antiresonances, and transmission spectra for a metasurface comprising rod-shaped resonators to suppress the S_0 mode – a study required to understand the widening of bandgaps. An equivalent study on topology-optimized resonators is presented to reiterate the connection between the resonator's resonances and antiresonances and the transmission spectrum, even for non-prismatic geometries, and to highlight the need for bandgap enhancement strategies. Section IIIA presents a topology optimization design methodology to conceive resonators that leads to wide bandgaps for the S_0 mode. Section IIIB presents the numerical validation and discusses its limitations for the resultant topology-optimized resonators when arranged as a metasurface. Finally, we present our conclusions in Section IV.

II. ROLE OF RESONANCES AND ANTIRESONANCES IN FORMING S_0 MODE BANDGAPS

In this section, we investigate the resonator-wave interactions using finite element analyses, which are useful to study not only simple prismatic shapes, but also non-prismatic, complex-shaped resonator topologies, as presented in the subsequent sections. To inform the optimization design of resonators to induce wide bandgaps - by tailoring resonances and antiresonances without considering the waveguide - we should address the following key questions. First, are resonances and antiresonances exhibited by the resonators preserved between the following two scenarios: (i) uncoupled resonator under in-plane unidirectional harmonic excitation at the resonator's base, mimicking the S_0 Lamb mode wave structure and (ii) resonator coupled to a plate excited with a propagating S_0 mode? Second, how well do these resonances and antiresonances map to the resultant bandgap width? Finally, do the relations between these resonances and antiresonances with the bandgap hold true for complex resonator geometries, such as the ones that commonly result from topology optimization? To answer these questions, two studies are presented below. The first study involves a prismatic rod-shaped resonator, and the second focuses on a non-prismatic topology-optimized resonator.

A. Prismatic rod-shaped resonators

Consider a metasurface to suppress the S_0 mode comprised of prismatic rod-shaped resonators, made of aluminum (Young's modulus = 69 GPa, density = 2800 kg/m^3 and Poisson's ratio = 0.3), with dimensions 7.9 mm × 7.9 mm × 23.4 mm, as shown in Fig. 1(a). To investigate the correspondence between the S_0 mode bandgap and the rod-shaped resonators' resonances and antiresonances, we simulate the response of the corresponding metasurface using frequency-domain analysis in COMSOL Multiphysics (v6.1) followed by laboratory experiments on a 1 mm-thick aluminum plate. Following our previous work [30], [31], the finite element model is divided into several regions: an excitation region of length λ, an incident region of length λ, a metasurface region of length 7 cm having three rows of resonators with 10 resonators in each row and a lattice length of 11 mm, and a transmission region of length 4λ, as shown in Fig. 1(a), where λ is the S_0 mode wavelength at each excitation frequency (20-140 kHz). Perfect contact between the resonators and the plate is assumed, disregarding any bonding effects. The surrounding $\lambda/4$ wide perfectly matched absorbing layers are used to prevent reflections from the model boundaries. To selectively excite a pure S_0 mode, a body load applies the S_0 mode wave structure over the excitation region for each excitation frequency sweeping from 20 kHz to 140 kHz in steps of ~1.4 kHz. Further details on the body-load excitation used in this study can be found in the Appendix A. To ensure mesh convergence, 3D brick and tetrahedral elements with a maximum mesh size of ~$\lambda_{min}/8$ are used, where λ_{min} refers to the smallest possible wavelength of a guided mode propagating in a 1 mm-thick aluminum plate at each excitation frequency; in this case, an A_0 mode. In this study, λ_{min} ranges from 22.3 mm at 20 kHz to 7.9 mm at 140 kHz.

The laboratory experiments are conducted on machined Aluminum rod-shaped resonators, which are glued to the plate using superglue in the same resonator arrangement as considered in the numerical study, as shown in Fig. 1(b). A 100 kHz Olympus shear transducer preferentially excites the S_0 mode, and a long-range Polytech laser doppler vibrometer (OFV-500) is used for reception, mounted to a micro-precision Newport scanning stage (ILS250PP, 250 mm scan length). The laser head is tilted 34 degrees with respect to the vertical plane to capture the contribution of both in-plane and out-of-plane particle velocities, using a retroreflective tape to enhance laser reflectivity. To cover the desired frequency range of 20-140 kHz, we use a broadband Ricker excitation pulse with central frequency at 50 kHz, and scan over 25 cm in the transmission region (marked in Fig. 1(b)) in steps of 0.25 cm. At each scanning step, 100 ultrasonic signals are recorded for 1000 us with a pulse-repetition frequency of 100 Hz and a sampling rate of 50 MHz and are subsequently averaged. Other parts of the data acquisition hardware include a National Instruments data acquisition system with a PXIe-5433 waveform generator and a PXIe-5172 oscilloscope cards, a TEGAM amplifier, and an Olympus pre-amplifier. Duct seal is applied around the plate edges to minimize side-wall reflections.

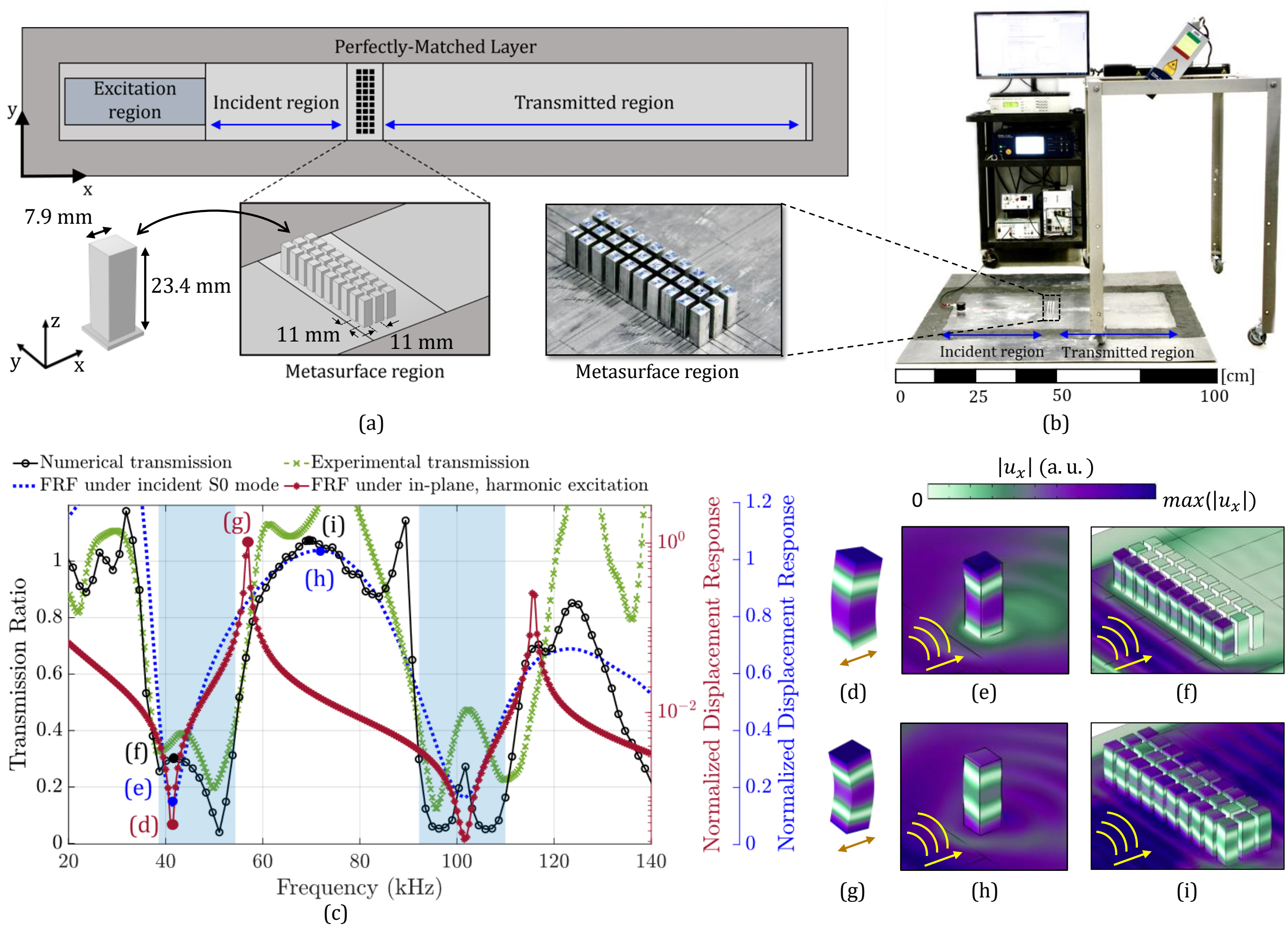

Figure 1: Numerical and experimental investigations of a metasurface comprising prismatic rod-shaped resonators. (a) Schematic of the finite element model used for frequency-domain analysis, and (b) the experimental setup for validation. (c) Frequency Response Function (FRF) at the resonator's base under unidirectional harmonic excitation for an uncoupled resonator (maroon line, dot markers) with subfigures (d) and (g) at 41.5 kHz and 57 kHz, respectively, FRF at the resonator's base under $\boldsymbol{S_0}$ mode wave propagation for a single resonator coupled to the plate (dashed blue line) with subfigures (e) and (h) at 41.5 kHz and 71.6 kHz, respectively, transmission spectra for numerical (black line, circular markers) with subfigures (f) and (i) at 41.5 kHz and 70.2 kHz, respectively, and transmission spectra obtained from experiments (green dashed line, cross markers). The shaded blue regions indicate the flexural-resonance bandgaps identified from dispersion analysis of the metasurface unit cell (see supplementary material). Subfigures or Mode shapes (d) to (i) show the in-plane displacement fields ($|\mathbf{u_x}|$) at their corresponding frequencies, highlighting the resonator and metasurface responses at the start and end of the first flexural-resonance bandgap.

Fig. 1(c) compares numerical and experimental response of a metasurface comprised of rod-shaped resonators. Three sets of results are presented: (i) the displacement response of the resonator to in-plane harmonic forces, (ii) the displacement response of a single resonator mounted on the plate under incident S_0 mode, and (iii) metasurface transmission spectra, both numerical and experimental. For the resonator's displacement responses, the in-plane displacement responses ($|\mathbf{u_x}|$) at the resonator's base in both configurations are overlaid in Fig. 1(c), including subfigures Figs. 1(d), 1(e), 1(g) and 1(h). The displacement responses for the resonator mounted on the plate are normalized by those extracted at the same point in a baseline simulation (plate without the resonator). The transmission spectra in Fig. 1(c) are calculated by normalizing the spectral amplitude peak of the transmitted S_0 mode by the same quantity obtained for a baseline case without the metasurface in place. All spectral amplitudes are obtained by applying the spatial Fast Fourier Transform (FFT) to the complex displacement data ($\mathbf{u_x} + \mathbf{u_y} + \mathbf{u_z}$), extracted over the transmission region (refer to Fig. 1(a)) on the surface, at the center of the plate for each excitation frequency. In the case of experiments, it is common for shear transducers to excite both S_0 and A_0 modes, which may influence the transmission ratio. Consequently, we first filter the raw A-scans to remove contributions from the incident A_0 mode on the metasurface before performing a 2D space-time FFT over the received data in the transmission region (refer to Fig. 1(b)) to decompose the transmitted wave modes into S_0 and mode-converted A_0 modes. The transmission spectrum is produced by extracting the spectral amplitude peak of the transmitted S_0 mode from the 2D-FFT wavenumber-frequency dispersion spectra and normalizing it by that obtained from the baseline measurements. Additional details on the data processing steps to obtain the transmission spectra from the experiment is provided in the supplementary material.

The two transmission spectra obtained numerically and experimentally align well, demonstrating the efficacy of the numerical models and the experimental setup used. Moreover, these plots reveal the frequency regions where transmission drops coincide with the flexural-resonance bandgaps, as identified through the dispersion analyses (shaded in blue), provided in the supplementary material. For instance, the first and second frequency bandgaps identified from the dispersion analysis from 38.6 - 54.4 kHz and 92.2 - 110 kHz, respectively, corresponds closely to the 50% numerical transmission ratio drop in Fig. 1(c) from 36.3 - 55.2 kHz and 91.4 - 112.8 kHz, respectively. Additionally, the resonator's flexural antiresonance frequencies under in-plane harmonic excitation or incident S_0 mode, identified at 41.5 kHz and 101.5 kHz for both the excitation scenarios in Fig. 1(c) are close to the start of the bandgaps observed in the transmission analysis (36.3 kHz and 91.4 kHz at the 50% threshold). Also, note that the mode shapes observed at the antiresonance frequency (Fig. 1(d) for in-plane harmonic excitation and Fig. 1(e) for the incident S_0 mode) match to mode shapes (Fig. 1(f)) at a point observed within the transmission drop shown in Fig. 1(c), demonstrating a strong connection between harmonic responses and transmission plots, similar to previous findings in the context of A_0 mode [23]. Although the antiresonance frequencies do not perfectly match the bandgap’s start, we argue that the bandgap starts when the displacement response ($|\mathbf{u_x}|$) at the waveguide’s surface resembles a clamping-like condition occurring before the antiresonance fully develops. Nonetheless, the resonator’s antiresonances clearly indicate that a bandgap has started even if the exact starting frequency is not known from the FRFs. Dispersion analyses or transmission spectra could yield a precise bandgap starting frequency at the expense of computation time. Note that the antiresonances of a resonator under a harmonic excitation are equivalent to the resonator’s eigenfrequencies upon constraining the degrees of freedom along the direction in which the harmonic load would be applied; these displacement-constrained eigenfrequencies are referred to as *antiresonance eigenfrequencies*. Consequently, the antiresonance frequencies obtained under either in-plane harmonic excitation or incident S_0 mode, can also be viewed as the antiresonance eigenfrequencies of the resonator when the in-plane particle motion at its base is clamped, and therefore are independent of the waveguide.

On the other hand, the resonator’s flexural resonances at 57 kHz and 115.5 kHz under in-plane harmonic excitation correspond to the eigenfrequencies of the resonator when no degrees of freedom are constrained (*resonance eigenfrequencies*) and are also independent of the waveguide. These resonances are identified in Fig. 1(c) and align close to the end of the first and second bandgaps observed in the transmission spectra in Fig. 1(c) at 55.2 kHz and 112.8 kHz (50% threshold). Note that despite the close resemblance of the mode shapes (Figs. 1(g) and 1(h)), the resonance frequencies identified under an incident S_0 mode do not perfectly align with those identified under in-plane harmonic excitation but instead appear at slightly higher frequencies. These frequencies, also referred to as coupling resonance frequencies, are an indirect consequence of the waveguide-resonator coupling and require solving a complex boundary value problem for analytical estimation. These resonance frequencies provide a more accurate estimate of the upper bound of the S_0 mode bandgap compared to the resonance frequencies under in-plane harmonic excitation, as they align well with the maxima in the transmission spectra at the bandgap ends, similar to that observed for A_0 mode [23].

A key finding of the above analysis is that ensuring bandgap formation at a target frequency necessitates aligning the waveguide-independent antiresonance frequencies of the resonators to the desired target frequency. However, accurately estimating the true extent of the bandgap requires identifying the resonance frequency of the resonator subject to incident S_0 mode, which requires accounting for the waveguide. Notably, the displacement responses under both excitation scenarios - unidirectional harmonic and incident S_0 mode – exhibit similar trends. In fact, the resonator's resonance displacement fields under both excitation scenarios (Figs 1(g) and 1(h)) match the mode shape at the maximum in the transmission spectra (Fig 1(i)). This observation suggests that controlling the waveguide-independent resonance frequency under unidirectional harmonic excitation could indirectly influence the resonance frequency under an incident S_0 mode, suggesting that a design methodology of resonators for locally resonant metasurfaces does not need to necessarily consider the resonator-waveguide interactions; the waveguide can be disregarded, thus, simplifying the design process and minimizing the computational complexity. Based on these observations, it is feasible to design a resonator that induces a wide bandgap solely by forcing its resonances to move away from the antiresonances considering only the in-plane harmonic excitation. It is important to note, however, that while excluding the waveguide simplifies the design process, it does not allow for an accurate estimation of the bandgap width, which is influenced by the relative inertia between the waveguide and resonator [26]. Thus, soft or stiff waveguides influence the width of the bandgap by shifting the upper bound of the bandgap to higher or lower frequencies, as illustrated in the supplementary material (See Fig SM2 and related discussions). Nevertheless, for a given waveguide, such a resonator design strategy could enable designs for wider bandgaps. However, it remains crucial to establish whether the connections observed above apply to complex resonator topologies such as non-prismatic shapes or those typically obtained from topology optimization [30], which exhibit modes beyond simple longitudinal and flexural modes.

B. Non-prismatic elephant-shaped resonators

In earlier topology optimization studies, we exploited the single antiresonance matching approach [30] to design an elephant-shaped resonator that yielded an S_0 bandgap at the specified target frequency of 50 kHz, and the double antiresonance matching approach [31] to design a turkey-shaped resonator, which yielded a surface-mode bandgap at the target frequency of 30 kHz. As an example of non-prismatic resonators, we revisit and investigate the response of aluminum-made elephant-shaped resonator, as illustrated in Fig 2(a). We follow similar analyses as previously discussed for rod-shaped resonators to study the relation among resonances, antiresonances, and bandgaps from transmission spectra. In a square lattice, the required lattice length would exceed 25 mm, preventing a closely spaced arrangement of the resonators that is crucial for achieving significant bandgap width [24]. Instead, we employ four rows of staggered, closely packed elephant-shaped resonators, with a distance of 14.5 mm between each row and a spacing of 34 mm between resonators within each row, mounted on a 1 mm-thick aluminum plate for both numerical and experimental tests, as shown in Figs 2(b) and 2(c), respectively.

We consider the same numerical model presented in Fig. 1(a), experimental setup as in Fig. 1(b), and procedure for data processing as described in Section II-A for the rod-shaped resonators. The elephant-shaped resonators were 3D-printed with Aluminum alloy (AlSi10Mg) using Selective Laser Melting with the following process parameters: 30 μm layer thickness, 25-70 μm particle size, and 300W laser power. The resonators' material properties were estimated from air-coupled resonance ultrasound spectroscopy tests (Young's modulus= 70 GPa, density = 2700 kg/m^3, and Poisson's ratio = 0.33) by minimizing the error between the measured and simulated free-free resonances, employing a genetic algorithm-based optimization routine [32]. Due to the rough surfaces of the 3D-printed resonators, their bases were first carefully smoothed using sandpaper to ensure a better contact surface for bonding. The resonators were then individually glued to the plate by applying pressure. The numerical and experimental transmission spectra agree well up to 100 kHz, above which there is insufficient excitation amplitude. However, we note that the bandgaps from numerical analysis are sharper compared to those from experimental analysis, and the two closely spaced bandgaps around 80-100 kHz merge into a single bandgap in the experiments. These subtle discrepancies are likely due to imperfections in resonator bonding and surface roughness of the 3D-printed resonators, as well as inaccuracies during the additive manufacturing process. Additionally, material or geometrical damping, which is not accounted for in the numerical analysis, may contribute to the broader bandgaps observed in the experiments. Despite these issues, the transmission spectra effectively demonstrate the effectiveness of the locally resonant metasurface in preventing the propagation of S_0 waves using topology-optimized resonators.

For a single elephant-shaped resonator, the in-plane displacement responses ($|\mathbf{u_x}|$) extracted at the resonator's base subject to unidirectional harmonic excitation and incident S_0 mode are superimposed over the transmission spectra in Fig. 2(d) for comparison. One of the sharp dips in the in-plane displacement response at the resonator's base (i.e., the antiresonances), shown in Fig. 2(d), corresponds to the optimized antiresonance frequency at 50 kHz. Although antiresonances (incident S_0 mode – 25 kHz, 52.4 kHz, 73 kHz, and 88 kHz; and in-plane harmonic excitation – 24.5 kHz, 51.5 kHz, 71.5 kHz, 87.5 kHz) and resonances (incident S_0 mode – 49.7 kHz, 70.2 kHz, 83.9 kHz, and 93.5 kHz; and harmonic excitation – 44.5 kHz, 66.5 kHz, 76.5 kHz, and 91 kHz) for both excitation types do not perfectly align, the displacement responses exhibit a consistent trend. Notably, the antiresonance-resonance pairs closely bound the resulting bandgaps observed in the transmission analysis, which is similar to the observations for rod-shaped resonators. For example, the first two bandgaps reveal that the antiresonance frequencies for both excitation types (incident S_0 mode – 25 kHz and 52.4 kHz; and harmonic excitation – 24.5 kHz and 51.5 kHz) closely match the starting of the numerical transmission dips seen in simulations (20.8 kHz and 50.5 kHz at 50% threshold). Additionally, the resonance frequencies for both excitations (incident S_0 mode – 49.7 kHz and 70.2 kHz; and harmonic excitation – 44.5 kHz and 66.5 kHz) align closely with the maxima in the numerical transmission spectra (48.3 kHz and 64.8 kHz). Moreover, the mode shapes at the target antiresonance frequency, which exhibit displacement clamping at the resonator base for both excitation types (in-plane harmonic – Fig. 2(e); incident S_0 mode – Fig. 2(f)), match the clamping condition observed at the base of resonators in the metasurface at frequencies within the transmission dip (51.1 kHz, Fig. 2(g)). Similarly, the mode shapes at the resonance frequencies, show significant displacement at the resonator base for both excitation types (in-plane harmonic – Fig. 2(h); incident S_0 mode – Fig. 2(i)) like the resonator response near the transmission maxima (64.8 kHz, Fig. 2(j)). This correspondence demonstrates that a constrained-like in-plane displacement (i.e., an antiresonance) at the plate's surface leads to S_0 mode suppression even for complex non-prismatic resonators and that analyzing an individual resonator without considering the waveguide interaction is a feasible design approach to tailor frequency bandgaps for locally resonant metasurfaces.

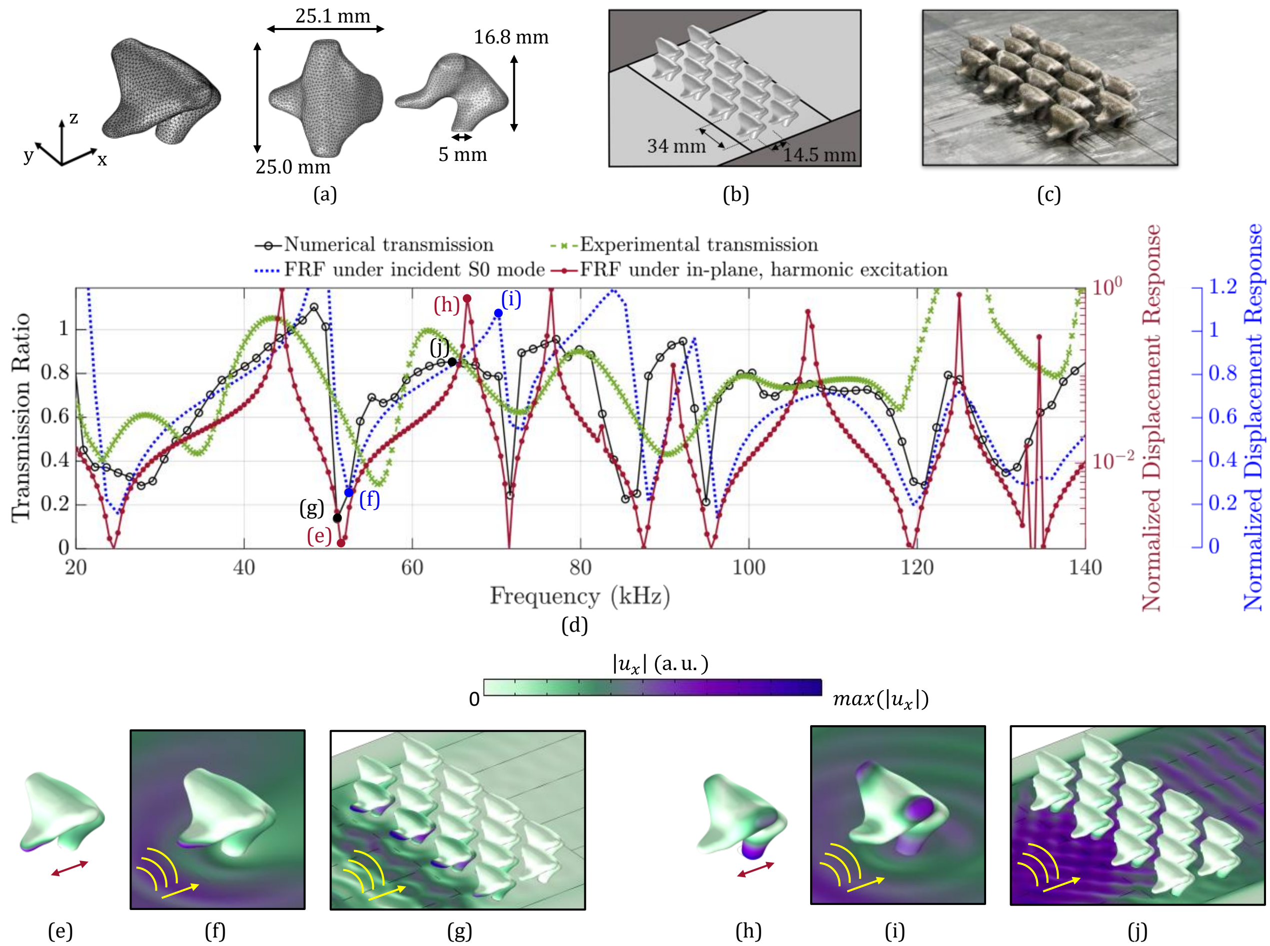

Figure 2: Numerical and experimental investigations of a metasurface comprising non-prismatic elephant-shaped resonators obtained through TO [30]. Close-up view of the (a) elephant-shaped resonator and the metasurface configuration in the (b) frequency-domain finite element model and (c) experimental setup. (d) Frequency Response Function (FRF) at the base of the resonator under unidirectional harmonic excitation for an uncoupled resonator (maroon line, dot markers) with mode shapes shown in subfigures (e) and (h) at 51.5 kHz and 66.5 kHz, respectively, FRF at the resonator's base under $\boldsymbol{S_0}$ mode wave propagation for a single resonator coupled to the plate (dashed blue line) with mode shapes shown in subfigures (f) and (i) at 52.4 kHz and 70.2 kHz, respectively, transmission spectra for numerical (black line, circular markers) with mode shapes shown in subfigures (g) and (j) at 51.1 kHz and 64.8 kHz, respectively, and transmission spectra obtained from experiments (green dashed line, cross markers). The snapshots in (e) to (j) show the in-plane displacement fields ($|\mathbf{u_x}|$) at their corresponding frequencies, highlighting the resonator and metasurface responses at the start and end of the second flexural-resonance bandgap.

One discrepancy is the observed formation of a very narrow second dip in the numerical transmission spectra (50.5 – 53.4 kHz at 50% threshold), despite the presence of an antiresonance at 51.5 kHz and a resonance at 66.5 kHz identified from the in-plane unidirectional loading. We believe this narrow dip is due to additional internal interactions among the staggered resonators, which exhibit other resonator modes when subjected to excitations in different directions. This may have occurred because the response to unidirectional harmonic loads only considers one excitation direction and does not account for resonances or antiresonances associated with other harmonic excitations. To address this issue, we propose to push all eigenfrequencies away from the desired frequency range, thereby mitigating the occurrence of spurious resonances, as will be demonstrated in the following sections. Although tailoring a resonator's antiresonances under harmonic excitation enables bandgap customization, as established through the elephant-shaped resonator analysis, the obtained bandgap around the optimized antiresonance frequency, 50 kHz, is very narrow compared to the metasurface comprising prismatic resonators. Thus, even for complex resonator topologies, the correspondence between the resonator's antiresonance and resonances with the start and end of bandgaps holds, suggesting a potential resonator design strategy to obtain wider bandgaps by pushing apart all resonance modes from the targeted antiresonance. This motivates a systematic design methodology based on topology optimization presented in subsequent sections.

III. TOPOLOGY OPTIMIZATION FOR BANDGAP ENHANCEMENT

The optimization problem is to systematically match an antiresonance frequency with a target frequency (the frequency around which the bandgap is desired) while simultaneously pushing all surrounding resonances away from that antiresonance frequency to generate a wide bandgap. This optimization problem is an extension of our earlier proposed methodology, i.e., generating bandgaps through single antiresonance matching as described in [30]. In this approach, the objective function minimizes the normalized difference between an antiresonance eigenfrequency f_A and a prescribed target frequency f_T, while maximizing the normalized difference between all resonance eigenfrequencies f_R and the antiresonance eigenfrequency f_A. The optimization problem is then defined as:

$$\min_{\boldsymbol{\rho}} \left[w_1 \left(\frac{f_A - f_T}{f_T} \right)^2 + w_2 \left| \frac{f_A}{f_R - f_A} \right| \right], \tag{1}$$

subject to:

$$\mathrm{V_{min}} \leq \sum_{\mathrm{e}=1}^{\mathrm{N_e}} \rho_\mathrm{e} \mathrm{V_e} \leq \mathrm{V_{max}} \tag{2a}$$

$$0 < \rho_{\mathrm{min}} \leq \rho_\mathrm{e} \leq 1, \tag{2b}$$

where ρ_e are the design variables, i.e., the pseudo-densities associated to the finite elements in the design space, and the weighting coefficients w_1 and w_2 control the contribution of the antiresonance matching and resonance gap terms in Eq. (1), respectively. $\mathrm{V_{min}}$ and $\mathrm{V_{max}}$ are the minimum and maximum volume constraints, considering that the factor $\rho_\mathrm{e}\mathrm{V_e}$ is the element-wise volume. The design variables ρ_e range from 0 to 1, however, a minimum limit ρ_{min} is imposed to prevent numerical errors. While minimizing the first term in the objective function aims to align the antiresonance eigenfrequency f_A with the target frequency f_T , the second term increases sharply as f_A approaches the resonance eigenfrequency f_R. This term attains its minimum value only when f_A and f_R are sufficiently spaced apart, thereby driving the resonance gap wider.

Two generalized eigenvalue problems ($\mathbf{K\Phi} = \boldsymbol{\lambda}\mathbf{M\Phi}$) are solved independently to obtain either resonance or antiresonance eigenfrequencies, using the appropriate displacement constraints for each case. Extensive details on how these eigenfrequencies are computed and selected during the optimization are presented in [33]. A Sequential Linear Programming (SLP) scheme is implemented to solve the optimization problem presented in Eq. (1) and Eq. (2), which requires the linearization of these equations. Since Eq. (2) already contains linear functions, only Eq. (1) is linearized using first-order Taylor series. The details of the derivation are presented in the Appendix B. Eq. (1) simplifies to:

$$\min_{\boldsymbol{\rho}}\left[\left(\frac{w_1(f_A-f_T)}{4\pi^2 f_A f_T^2}\frac{\partial\lambda_A}{\partial\rho_k}+\frac{w_2 f_A}{8\pi^2(f_R-f_A)^2}\left|\frac{f_R-f_A}{f_A}\right|\left[\frac{1}{f_A}\frac{\partial\lambda_A}{\partial\rho_k}-\frac{f_A\frac{\partial\lambda_R}{\partial\rho_k}}{f_R(f_R-f_A)}+\frac{\frac{\partial\lambda_A}{\partial\rho_k}}{(f_R-f_A)}\right]\right)\rho_k\right], \tag{3}$$

where:

$$\frac{\partial\lambda}{\partial\rho_k}=\frac{\Phi^T\left(\frac{\partial\boldsymbol{K}}{\partial\rho_k}-\lambda\frac{\partial\boldsymbol{M}}{\partial\rho_k}\right)\Phi}{\Phi^T\boldsymbol{M}\Phi}. \tag{4}$$

A. Case study

Here, we present an optimized resonator to constitute a locally resonant metasurface that controls the propagation of S_0 Lamb waves using the design methodology presented in the previous subsection. Ensuring feasible solutions throughout the optimization process is essential for convergence and numerical stability. This has been achieved by selecting the design domain dimensions and material properties shown in Table 1 such that the topology under harmonic excitation at each iteration has resonances and antiresonances in the frequency range from 10 kHz to 150 kHz.

TABLE I. Optimization initialization parameters

Target frequency f_T	50 kHz
Design domain	24 × 24 × 24 mm
Finite element size	1 mm
Young's modulus	69 GPa
Mass density	2730 kg/m^3
Poisson's ratio	0.33
Maximum volume constraint	$V_{max} = 50$ %
Minimum volume constraint	$V_{min} = 10$ %
Starting design variables	$\rho_e = 0.5$

To reduce computational complexity at each iteration, the design domain is assumed to be symmetric about the plane perpendicular to the harmonic excitation direction. The optimization runs until it reaches convergence; the evolution of the resonator's topology during the optimization process is shown in Fig. 4 at iterations 1, 10, 20, 30, 40, and 50 after recovering the symmetry condition. At the start of the optimization process (iteration 1), the distribution of material is homogeneous with a pseudo-density of 50% ($\rho_e = 0.5$) for all elements in the design domain, except those in the lowest row, which have been defined as void non-design elements with a fully-solid non-design region that constitutes the resonator's base that will be in contact with the plate. After minimizing the objective function and obtaining a local solution, the resultant optimized resonator is a "Lemon-shaped" topology that uses 18.8% of the volume fraction.

A frequency response subject to unidirectional harmonic forces must be computed at each iteration to properly identify resonances and antiresonances. Fig. 4 compares the topology's frequency response at the first, intermediate, and final iterations of the optimization as shown in Fig 3., indicative of the effectiveness of the proposed optimization strategy in matching an antiresonance with a target frequency (f_T) while pushing away all the surrounding resonances. At the first iteration, multiple resonances and antiresonances appear within the target frequency range; specifically, antiresonances occur at 19 kHz, 84 kHz, and 116 kHz, while resonances occur at 80 kHz, 106 kHz, 127 kHz. After reaching convergence at iteration 50, the antiresonance from 19 kHz has been shifted up to 49 kHz, with all resonances pushed out beyond the plotted frequency range. This ultra-wide frequency separation between the antiresonance and nearby resonances has a potential to generate wide frequency bandgaps once they are arranged as a locally resonant metasurface, as will be numerically validated in the subsequent section.

The proposed design methodology, which manipulates eigenfrequencies for both resonances and antiresonances, offers a substantial reduction in computational expense compared to traditional frequency response-based design methods. The computational cost of design optimization can be evaluated based on the time required for a single iteration during the optimization process. For example, in the case of the lemon-shaped resonator, each iteration takes approximately 960 seconds (~16 minutes) with a mesh consisting of 6,912 elements, 31,225 nodes, and 93,675 degrees of freedom. These computations were run in distributed mode across five nodes of a cluster, each powered by 2 × Intel(R) Xeon(R) Gold 6248R CPUs at 3.00 GHz. Although this cost is higher than that of typical eigenfrequency-based optimization methods, it remains significantly lower than any frequency domain-based approach, highlighting the computational efficiency of our methodology.

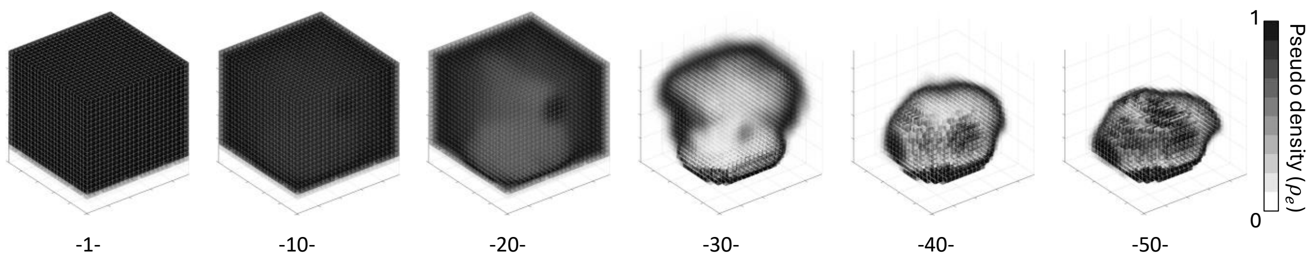

Figure 3: Optimization evolution, from left to right, showing the resultant topologies at iterations 1, 10, 20, 30, 40 and 50.

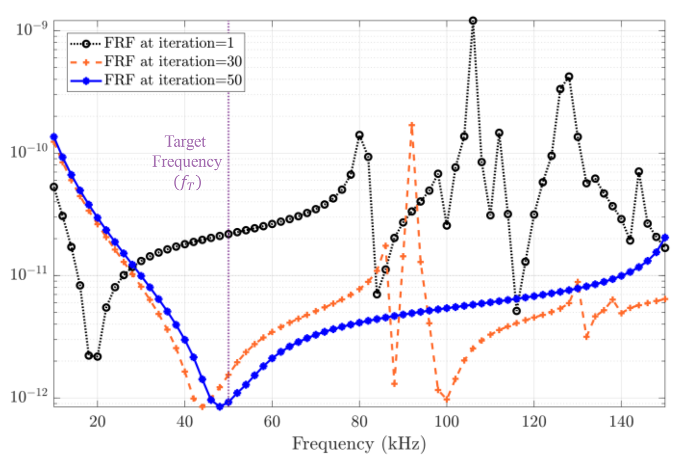

Figure 4: Frequency response functions for topologies at iterations 1, 30, and 50 from Fig. 3.

B. Numerical validation of topology-optimized resonator for ultra-wide bandgaps

The lemon-shaped optimized topology at iteration 50 in Fig. 3 is further post-processed to transform the pseudo-density values into a well-defined shape using the TOPslicer program [36], as shown in Fig 5(a). This post-processed topology's in-plane displacement response to unidirectional harmonic loading is shown in Fig. 5(b), which is comparable to the unprocessed topology's response shown in Fig. 3, illustrating that post-processing has minimal impact on the optimized resonator's response. To aid the comparison, the elephant-shaped topology's response to unidirectional in-plane harmonic loads from Fig. 2(d), is also included in Fig. 5(b). The differences between these two optimized topologies' frequency responses are evident. The lemon-shaped topology has a single antiresonance at 53.5 kHz, which is near the target frequency of 50 kHz, with significant separation between the antiresonance and the following resonance, at 137.5 kHz. On the other hand, the elephant-shaped topology, although having an antiresonance near the same target frequency, exhibits nearby resonances that are significantly closer to that antiresonance, resulting in narrower frequency bandgaps, as demonstrated in Section II.B. Following the same frequency-domain analysis presented in Section II for the rod-shaped and elephant-shaped resonators, the in-plane frequency response at the resonator's base for a single lemon-shaped resonator mounted on the plate subject to incident S_0 mode is also presented in Fig. 5(b). As expected, the observed antiresonance and resonance frequencies for both excitation cases match, so do their corresponding displacement fields in Figs. 5(c) to 5(f), confirming again the connection between resonances and antiresonances with and without coupling the resonator to the waveguide, i.e., the close correspondence between responses to unidirectional harmonic loads and the S_0 wave propagation. The wide frequency separation between the lemon-shaped resonator's antiresonance and resonances is expected to generate an ultra-wide S_0 mode bandgap, which is verified, as follows, with the frequency-domain transmission spectra plots.

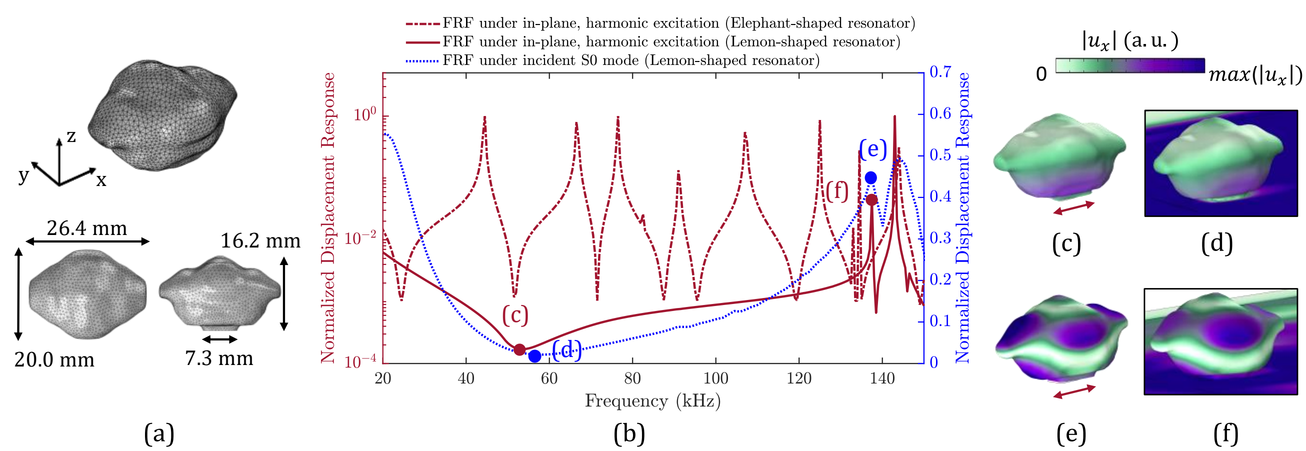

Figure 5: (a) The lemon-shaped optimized resonator after post-processing, and (b) the comparison of in-plane frequency response functions for the elephant-shaped and lemon-shaped resonators subject to unidirectional harmonic loading and to $\boldsymbol{S_0}$ wave mode. Displacement field $|\mathbf{u_x}|$ responses for the lemon-shaped resonator at the target antiresonances (shown in (c) and (d)), and at the resonances (shown in (e) and (f)).

The frequency-domain transmission analysis is performed over a metasurface comprised of a closely spaced, staggered arrangement of 16 lemon-shaped resonators with spacing similar to that employed earlier for the elephant-shaped resonators, as illustrated in Fig. 6(a). The lemon-shaped topology's numerical transmission spectrum in Fig. 6(b) indicates an S_0 mode bandgap spanning from 28.2 kHz to 72 kHz, corresponding to the frequency range when the transmission drops below the 50% threshold. The transmission analysis confirms initiation of the bandgap (28.2 kHz) before the resonator's antiresonance under harmonic excitation (marked as f_A in Fig 6(b)). This bandgap formation starting before the antiresonances is a result of preceding resonances being pushed away from that antiresonance during the optimization process, although the exact frequency at which the bandgap starts is not predictable from the resonator's frequency responses. On the other hand, the bandgap ends (72 kHz) before the resonance frequency (marked as f_R in Fig. 6(b)) that is expected to be the bandgap's upper bound. This discrepancy is attributed to the resonator arrangement, which introduces additional complexities. Despite forcing resonances away from the antiresonance, the observed premature rise in the transmission around 80 kHz is due to the resonator arrangement that gives rise to other propagating modes that limit the extent of bandgap up to the resonance frequency, like what was observed in the transmission bandgaps for elephant-shaped resonators (Fig 2(d)). The narrowing of bandgap, caused by wave scattering due to interactions between resonators within the designed frequency range (as shown in the supplementary material), is an indirect consequence of not considering the waveguide during the optimization process, as a compromise to enable the design of 3D topologies with feasible computational complexity.

Remarkably, despite the compromise in bandgap width, the lemon-shaped resonators (at 50% threshold) exhibit a bandgap approximately 15 times wider than that of the elephant-shaped resonators, as shown in Fig. 6(b). The filling fraction, representing the effective area covered by the metasurface, can be calculated as $\frac{\pi D^2}{2ab}$ for the centered rectangular Bravais lattice in the staggered resonator arrangement considered for this study. Here, a = 34 mm and b = 29 mm are the lengths of the lattice vectors (see Fig. 2(b)), while D is the diameter of the resonator base, approximated as a circle with dimensions D = 5 mm for the elephant-shaped resonator and D = 7.3 mm for the lemon-shaped resonator (see Figs. 2(a) and 5(a)). The higher filling fraction of the lemon-shaped metasurface (0.085) compared to that for elephant-shaped metasurface (0.04), along with its greater mass (9.8 g) relative to that of elephant-shaped resonators (6.2 g), are potential contributing factors to the observed enhanced bandgap, as suggested by previous studies [24], [26]. These results validate that the topology optimization approach based on antiresonances matching plus resonance gap enhancement results in metasurfaces exhibiting wider bandgaps compared to the optimization that focuses solely on antiresonance matching. We assert that a more densely packed arrangement of resonators could result in an even wider bandgap as predicted by the dispersion analysis over lemon-shaped resonators (see supplementary material) in which the antiresonance-to-resonance spacing resulted in a theoretical ultra-wide bandgap. While such a closely packed arrangement is impractical for the physical size of the lemon-shaped resonators, this analysis offers valuable insights into potential future directions for topology optimization, suggesting that imposing stricter volume constraints during resonator design could enable tighter configurations, potentially leading to significantly wider bandgaps.

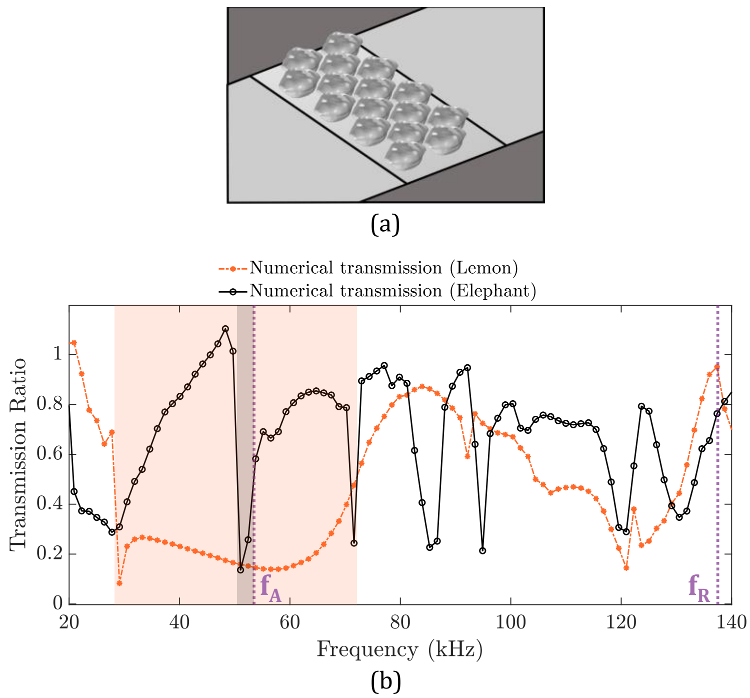

Figure 6: (a) Close-up view of the lemon-shaped metasurface configuration in the frequency-domain finite element model and (b) comparison of transmission spectra plots obtained from numerical simulations for elephant-shaped and lemon-shaped resonators. Bandgaps computed with 50% transmission drop threshold are highlighted in gray for elephant-shaped resonator arrangement and in orange for lemon-shaped resonator arrangement, and the antiresonance ($\boldsymbol{f_A}$) and resonance ($\boldsymbol{f_R}$) frequencies from the FRF for in-plane, harmonic excitation of lemon-shaped resonators are denoted by vertical lines for reference.

VI. Conclusions

Understanding the role of individual resonators' resonances and antiresonances in generating frequency bandgaps is crucial to proposing rational metasurface design approaches. In the context of suppressing an S_0 mode using a locally resonant metasurface, we demonstrated a strong connection between antiresonances and resonances of resonators coupled to a plate's surface subject to S_0 mode propagation, and antiresonances and resonances obtained by simple unidirectional in-plane harmonic excitations (mimicking S_0 mode wave structure) of an uncoupled resonator. These antiresonance and resonance frequencies match well, respectively, the start and end of frequency bandgaps, even for complex-shaped resonator topologies, demonstrating that the resonator-waveguide interactions can be disregarded during the resonator design process and motivating a new resonator design methodology that induces wider bandgaps by manipulating those resonances. To that end, we proposed a density-based topology optimization enforcing both the antiresonance matching and a new bandgap enhancement criterion based on resonance manipulation to force all nearby resonance eigenfrequencies away from the target antiresonance. This optimization technique converged to a lemon-shaped resonator topology for one set of selected initial conditions, which generated an S_0 mode bandgap around the target frequency that is significantly wider (15 times) than that of the elephant-shaped resonators.

This outcome validates our research objective of achieving a wider bandgap by incorporating the resonance gap enhancement term in the objective function, compared to the scenario that considers only antiresonance matching. This novel proposed optimization approach to obtain wide bandgaps at desired frequency ranges does not require consideration of the waveguide, eliminating the need for the parametric tuning of bandgaps through extensive dispersion analysis. This proposed waveguide-independent design methodology could be particularly useful to conceive metasurfaces for Rayleigh wave propagation control, where the waveguide (half-space) would require several finite element mesh elements, and is usually a complex and extensive computational task, especially when dispersion-based analysis is employed. However, the obtained bandgap for the optimized lemon-shaped resonators was narrower than predicted, primarily due to the size limitations of these resonators, which prevent the closely packed arrangement needed to achieve a complete bandgap spanning from antiresonance to resonance. This compromise arises from excluding the waveguide in the analysis to enhance computational efficiency while enabling metasurface designs with complex-shaped resonators in a 3D design space. Future work should focus on better understanding the scattering effects resulting from the arrangement of resonators that compromise the bandgap width, as well as strategies through topology optimization that could potentially induce an ultra-wide bandgap through volume constraints and close-packed configurations, with potential applications in surface-wave control.

SUPPLEMENTARY MATERIAL

See supplementary material for the dispersion analysis of rod-shaped resonators, influence of waveguide on bandgap characteristics, data analysis to obtain transmission spectra from experiments, dispersion analysis of topology-optimized lemon-shaped resonators, and evidence of the wave scattering interactions between resonators that compromise the desired frequency bandgap range.

ACKNOWLEDGMENTS

The authors gratefully acknowledge the support of the National Science Foundation under Grant No. 1934527. Any opinions, findings, and conclusions or recommendations expressed in this material are those of the author(s) and do not necessarily reflect the views of the National Science Foundation.

The authors gratefully thank Luke B. Beardslee from Los Alamos National Laboratory for his support on material characterization of 3D-printed elephant-shaped resonators.

Computations for this research were performed on the Pennsylvania State University's Institute for Computational and Data Sciences' Roar supercomputer.

AUTHOR DECLARATIONS

The authors have no conflicts to disclose.

DATA AVAILABILITY STATEMENT

The data that support the findings of this study are available from the corresponding author upon reasonable request.

APPENDIX A. NUMERICAL PROCEDURE TO PREFERNETIALLY EXCITE S_0 MODE IN A PLATE

Since the optimized topology designs discussed in the paper are specifically tailored to suppress the S_0 mode, it is crucial to study the interactions of the S_0 mode with the resonator topologies in isolation, without the interference of other guided modes that may be excited in the plate. To preferentially excite the S_0 mode, as briefly mentioned in [28], we employ body load excitation. Assuming wave propagation in the x-direction and plate thickness in the z-direction, as illustrated in Fig. 1(a), this method involves applying the stress distribution components ($\sigma_{xx}(z)$, $\sigma_{xy}(z)$, $\sigma_{xz}(z)$, $\sigma_{yy}(z)$, $\sigma_{yz}(z)$, and $\sigma_{zz}(z)$) along the plate thickness (z) of the S_0 mode, identified for each excitation frequency (20 kHz – 140 kHz in steps of ~1.4 kHz), as body loads (F_x, F_y, and F_z) to an excitation region spanning one wavelength of the wave propagating at the corresponding frequencies, as given by:

$$\begin{aligned} F_x &= \left(\sigma_{xx}(z) + \sigma_{xz}(z) + \sigma_{xy}(z)\right) e^{-i(k_x x - \omega t)}, \\ F_y &= \left(\sigma_{yy}(z) + \sigma_{yx}(z) + \sigma_{yz}(z)\right) e^{-i(k_x x - \omega t)}, \\ F_z &= \left(\sigma_{zx}(z) + \sigma_{zy}(z) + \sigma_{zz}(z)\right) e^{-i(k_x x - \omega t)}, \end{aligned} \tag{A1}$$

where k_x is the wavenumber in the direction of wave propagation and ω is the angular frequency.

The stress distributions of the S_0 mode at each excitation frequency can be identified using various techniques: solving the Navier governing equations analytically with traction-free boundary conditions on the surface [37], employing semi-analytical finite element analysis [38], or extracting them from dispersion analysis performed on a unit cell comprising a small portion of the plate with Bloch-Floquet periodic boundary conditions applied to the faces in the direction of wave propagation [39]. In this work, we used the latter approach to extract the dispersion curves of the Lamb modes (plotted as gray dotted lines in Fig. 7 and the corresponding stress distribution of the S_0 mode along the plate thickness. These stress distributions are then used as excitation loads, as detailed in the procedure above, for the frequency domain analysis presented in Figs. 1, 2, 5, and 6. For reference, the wavenumber spectrum was extracted by applying a spatial FFT over the complex displacement data ($u_x + u_y + u_z$) in the transmission region for the baseline case (i.e., without any surface-mounted resonators) and overlaid on the dispersion curves of the fundamental S_0, A_0 and SH_0 modes for all excitation frequencies, as illustrated in Fig 7. This figure illustrates the capability of the body load excitation to preferentially excite the S_0 mode, as evidenced by the fact that all wavenumber peaks coincide with the S_0 mode dispersion curve, with no visible peaks along the A_0 mode and low amplitude peaks observed along the SH_0 mode.

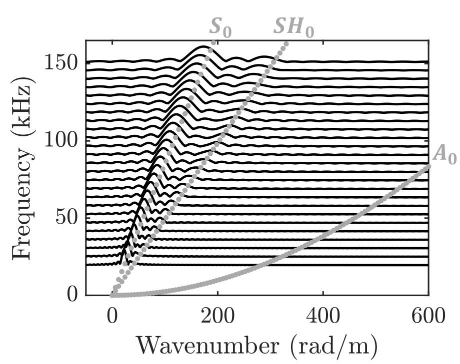

Figure 7: Wavenumber spectrum extracted from the transmission region without surface-mounted resonators for S_0 mode body-load excitation, overlaid on the dispersion curves of the A_0, S_0, and SH_0 modes across the 20 kHz to 140 kHz frequency range.

APPENDIX B. SENSITIVITY DERIVATION FOR THE OPTIMIZATION PROBLEM

A gradient-based optimization problem requires the derivation of its objective function with respect to the design variables. The present study employs the Sequential Linear Programming (SLP) method, which only requires the first derivative with respect to the design variables. To achieve such a purpose, first-order Taylor series are used, disregarding constant terms. For any objective function:

$$\min_{\rho}[\mathrm{f}(\rho)], \tag{B1}$$

its first-order Taylor series decomposition is:

$$\min_{\rho}[\mathrm{f}(\rho_0) + \nabla \mathrm{f}(\rho_0)^{\mathrm{T}}(\rho - \rho_0)]. \tag{B2}$$

Disregarding constant terms, the objective function simplifies to:

$$\min_{\rho}[\nabla \mathrm{f}(\rho_0)^{\mathrm{T}}(\rho)], \tag{B3}$$

where:

$$\nabla \mathrm{f}(\rho_0) = \left.\frac{\partial \mathrm{f}(\rho)}{\partial \rho_{\mathrm{k}}}\right|_{\rho_o}. \tag{B4}$$

Here ρ_0 is the linearization point, i.e., the current vector of pseudo-sensitivities at each iteration during the optimization process. The objective function from Eq. (1) is written as:

$$\min_{\rho}\left[\mathrm{w}_1\left(\frac{\mathrm{f_A} - \mathrm{f_T}}{\mathrm{f_T}}\right)^2 + \mathrm{w}_2\left|\frac{\mathrm{f_A}}{\mathrm{f_R} - \mathrm{f_A}}\right|\right]. \tag{B5}$$

The objective function linearized at ρ_0 can be written as:

$$\min_{\rho} \nabla \mathrm{f}(\rho_0)^{\mathrm{T}}\rho = \min_{\rho}\left.\frac{\partial \mathrm{f}(\rho)}{\partial \rho_{\mathrm{k}}}\right|_{\rho_o}\rho_{\mathrm{k},} \tag{B6}$$

where:

$$\begin{aligned}
\frac{\partial \mathrm{f}(\rho)}{\partial \rho_{\mathrm{k}}} &= \mathrm{w}_1\frac{\partial}{\partial \rho_{\mathrm{k}}}\left(\frac{\mathrm{f_A} - \mathrm{f_T}}{\mathrm{f_T}}\right)^2 + \mathrm{w}_2\frac{\partial}{\partial \rho_{\mathrm{k}}}\sqrt{\left(\frac{\mathrm{f_A}}{\mathrm{f_R} - \mathrm{f_A}}\right)^2} \\
&= 2\mathrm{w}_1\left(\frac{\mathrm{f_A} - \mathrm{f_T}}{\mathrm{f_T}}\right)\frac{\partial}{\partial \rho_{\mathrm{k}}}\left(\frac{\mathrm{f_A} - \mathrm{f_T}}{\mathrm{f_T}}\right) + \frac{1}{2}\mathrm{w}_2\left[\left(\frac{\mathrm{f_A}}{\mathrm{f_R} - \mathrm{f_A}}\right)^2\right]^{-\frac{1}{2}}\frac{\partial}{\partial \rho_{\mathrm{k}}}\left(\frac{\mathrm{f_A}}{\mathrm{f_R} - \mathrm{f_A}}\right)^2 \\
&= \frac{2\mathrm{w}_1(\mathrm{f_A} - \mathrm{f_T})}{\mathrm{f_T^2}}\frac{\partial(\mathrm{f_A} - \mathrm{f_T})}{\partial \rho_{\mathrm{k}}} + \frac{\mathrm{w}_2}{2}\sqrt{\left(\frac{\mathrm{f_R} - \mathrm{f_A}}{\mathrm{f_A}}\right)^2}\frac{\partial}{\partial \rho_{\mathrm{k}}}\left(\frac{\mathrm{f_A}}{\mathrm{f_R} - \mathrm{f_A}}\right)^2 \\
&= \frac{2\mathrm{w}_1(\mathrm{f_A} - \mathrm{f_T})}{\mathrm{f_T^2}}\frac{\partial(\mathrm{f_A})}{\partial \rho_{\mathrm{k}}} + \frac{\mathrm{w}_2}{2}\sqrt{\left(\frac{\mathrm{f_R} - \mathrm{f_A}}{\mathrm{f_A}}\right)^2}\,2\left(\frac{\mathrm{f_A}}{\mathrm{f_R} - \mathrm{f_A}}\right)\frac{\partial}{\partial \rho_{\mathrm{k}}}\left(\frac{\mathrm{f_A}}{\mathrm{f_R} - \mathrm{f_A}}\right).
\end{aligned} \tag{B7}$$

The last term in the derivative can be written as:

$$\frac{\partial}{\partial \rho_{\mathrm{k}}}\left(\frac{\mathrm{f_A}}{\mathrm{f_R} - \mathrm{f_A}}\right) = \frac{\frac{\partial \mathrm{f_A}}{\partial \rho_{\mathrm{k}}}(\mathrm{f_R} - \mathrm{f_A}) - \mathrm{f_A}\frac{\partial(\mathrm{f_R} - \mathrm{f_A})}{\partial \rho_{\mathrm{k}}}}{(\mathrm{f_R} - \mathrm{f_A})^2} = \frac{\frac{\partial \mathrm{f_A}}{\partial \rho_{\mathrm{k}}}}{(\mathrm{f_R} - \mathrm{f_A})} - \frac{\mathrm{f_A}\frac{\partial \mathrm{f_R}}{\partial \rho_{\mathrm{k}}}}{(\mathrm{f_R} - \mathrm{f_A})^2} + \frac{\mathrm{f_A}\frac{\partial \mathrm{f_A}}{\partial \rho_{\mathrm{k}}}}{(\mathrm{f_R} - \mathrm{f_A})^2}. \tag{B8}$$

Plugging in back to the derivation (Eq. (B7)), we get:

$$\begin{aligned}\frac{\partial f(\rho)}{\partial \rho_k} &= \frac{2w_1(f_A - f_T)}{f_T^2}\frac{\partial f_A}{\partial \rho_k} \\ &+ \frac{w_2}{2}\sqrt{\left(\frac{f_R - f_A}{f_A}\right)^2}\, 2\left(\frac{f_A}{f_R - f_A}\right)\left[\frac{\frac{\partial f_A}{\partial \rho_k}}{(f_R - f_A)} - \frac{f_A\frac{\partial f_R}{\partial \rho_k}}{(f_R - f_A)^2} + \frac{f_A\frac{\partial f_A}{\partial \rho_k}}{(f_R - f_A)^2}\right] \\ &= \frac{2w_1(f_A - f_T)}{f_T^2}\frac{\partial f_A}{\partial \rho_k} + \frac{w_2 f_A}{(f_R - f_A)^2}\sqrt{\left(\frac{f_R - f_A}{f_A}\right)^2}\left[\frac{\partial f_A}{\partial \rho_k} - \frac{f_A\frac{\partial f_R}{\partial \rho_k}}{(f_R - f_A)} + \frac{f_A\frac{\partial f_A}{\partial \rho_k}}{(f_R - f_A)}\right].\end{aligned} \tag{B9}$$

Now, knowing that eigenvalues and eigenfrequencies are related by:

$$\frac{\partial f_n}{\partial \rho_k} = \frac{1}{2\pi}\frac{\partial\sqrt{\lambda_n}}{\partial \rho_k} = \frac{1}{4\pi\sqrt{\lambda_n}}\frac{\partial \lambda_n}{\partial \rho_k} = \frac{1}{8\pi^2 f_n}\frac{\partial \lambda_n}{\partial \rho_k}, \tag{B10}$$

the objective function derivative simplifies to:

$$\begin{aligned}\frac{\partial f(\rho)}{\partial \rho_k} &= \frac{2w_1(f_A - f_T)}{8\pi^2 f_A f_T^2}\frac{\partial \lambda_A}{\partial \rho_k} + \frac{w_2 f_A}{(f_R - f_A)^2}\sqrt{\left(\frac{f_R - f_A}{f_A}\right)^2}\left[\frac{1}{8\pi^2 f_A}\frac{\partial \lambda_A}{\partial \rho_k} - \frac{\frac{f_A}{8\pi^2 f_R}\frac{\partial \lambda_R}{\partial \rho_k}}{(f_R - f_A)} + \frac{\frac{f_A}{8\pi^2 f_A}\frac{\partial \lambda_A}{\partial \rho_k}}{(f_R - f_A)}\right] \\ &= \frac{w_1(f_A - f_T)}{4\pi^2 f_A f_T^2}\frac{\partial \lambda_A}{\partial \rho_k} + \frac{w_2 f_A}{8\pi^2(f_R - f_A)^2}\sqrt{\left(\frac{f_R - f_A}{f_A}\right)^2}\left[\frac{1}{f_A}\frac{\partial \lambda_A}{\partial \rho_k} - \frac{f_A\frac{\partial \lambda_R}{\partial \rho_k}}{f_R(f_R - f_A)} + \frac{\frac{\partial \lambda_A}{\partial \rho_k}}{(f_R - f_A)}\right].\end{aligned} \tag{B11}$$

Finally, rewriting the optimization problem as presented in Eq. (3):

$$\min_{\boldsymbol{\rho}}\left[\left(\frac{w_1(f_A - f_T)}{4\pi^2 f_A f_T^2}\frac{\partial \lambda_A}{\partial \rho_k} + \frac{w_2 f_A}{8\pi^2(f_R - f_A)^2}\left|\frac{f_R - f_A}{f_A}\right|\left[\frac{1}{f_A}\frac{\partial \lambda_A}{\partial \rho_k} - \frac{f_A\frac{\partial \lambda_R}{\partial \rho_k}}{f_R(f_R - f_A)} + \frac{\frac{\partial \lambda_A}{\partial \rho_k}}{(f_R - f_A)}\right]\right)\rho_k\right]. \tag{B12}$$

REFERENCES

[1] P. Deymier, *Acoustic Metamaterials and Phononic Crystals (Springer Series in Solid-State Sciences)*, vol. 173. 2013.

[2] M. I. Hussein, M. J. Leamy, and M. Ruzzene, "Dynamics of phononic materials and structures: Historical origins, recent progress, and future outlook," *Appl. Mech. Rev.*, vol. 66, no. 4, 2014, doi: 10.1115/1.4026911.

[3] C. Charles, B. Bonello, and F. Ganot, "Propagation of guided elastic waves in 2D phononic crystals," *Ultrasonics*, vol. 44, no. SUPPL., 2006, doi: 10.1016/j.ultras.2006.05.096.

[4] N. Fang *et al.*, "Ultrasonic metamaterials with negative modulus," *Nat. Mater.*, vol. 5, no. 6, pp. 452–456, 2006, doi: 10.1038/nmat1644.

[5] P. Sheng, X. X. Zhang, Z. Liu, and C. T. Chan, "Locally resonant sonic materials," *Phys. B Condens. Matter*, vol. 338, no. 1–4, pp. 201–205, 2003, doi: 10.1016/S0921-4526(03)00487-3.

[6] A. Colombi, D. Colquitt, P. Roux, S. Guenneau, and R. V. Craster, "A seismic metamaterial: The resonant metawedge," *Sci. Rep.*, vol. 6, 2016, doi: 10.1038/srep27717.

[7] Muhammad, C. W. Lim, and K. Kamil Żur, "Wide Rayleigh waves bandgap engineered metabarriers for ground born vibration attenuation," *Eng. Struct.*, vol. 246, p. 113019, Nov. 2021, doi: 10.1016/j.engstruct.2021.113019.

[8] R. Zaccherini *et al.*, "Locally Resonant Metasurfaces for Shear Waves in Granular Media," *Phys. Rev. Appl.*, vol. 13, no. 3, Feb. 2020, doi: 10.1103/PhysRevApplied.13.034055.

[9] Z. Liu, K.-Q. Qin, and G.-L. Yu, "Partially Embedded Gradient Metabarrier: Broadband Shielding from Seismic Rayleigh Waves at Ultralow Frequencies," *J. Eng. Mech.*, vol. 146, no. 5, p. 04020032, 2020, doi: 10.1061/(asce)em.1943-7889.0001752.

[10] L. S. S. Pillarisetti, C. J. Lissenden, and P. Shokouhi, "Partially embedded metabarrier to suppress surface waves in granular media," *J. Acoust. Soc. Am.*, vol. 156, no. 3, pp. 1594–1608, 2024, doi: 10.1121/10.0028536.

[11] W. Li, F. Meng, Y. Chen, Y. fan Li, and X. Huang, "Topology Optimization of Photonic and Phononic Crystals and Metamaterials: A Review," *Adv. Theory Simulations*, vol. 2, no. 7, p. 1900017, Jul. 2019, doi: 10.1002/adts.201900017.

[12] G. Yi and B. D. Youn, "A comprehensive survey on topology optimization of phononic crystals," *Struct. Multidiscip. Optim.*, vol. 54, no. 5, pp. 1315–1344, 2016, doi: 10.1007/s00158-016-1520-4.

[13] S. Halkjær, O. Sigmund, and J. S. Jensen, "Maximizing band gaps in plate structures," *Struct. Multidiscip. Optim.*, vol. 32, no. 4, pp. 263–275, 2006, doi: 10.1007/s00158-006-0037-7.

[14] S. J. Cox and D. C. Dobson, "Maximizing band gaps in two-dimensional photonic crystals," *SIAM J. Appl. Math.*, vol. 59, no. 6, pp. 2108–2120, 1999, doi: 10.1137/s0036139998338455.

[15] C. Y. Kao, S. Osher, and E. Yablonovitch, "Maximizing band gaps in two-dimensional photonic crystals by using level set methods," *Appl. Phys. B Lasers Opt.*, vol. 81, no. 2–3, pp. 235–244, 2005, doi: 10.1007/s00340-005-1877-3.

[16] O. Sigmund and J. Sø. Jensen, "Systematic design of phononic band-gap materials and structures by topology optimization," *Philos. Trans. R. Soc. A Math. Phys. Eng. Sci.*, vol. 361, no. 1806, pp. 1001–1019, 2003, doi: 10.1098/rsta.2003.1177.

[17] J. Jung, S. Goo, and J. Kook, "Design of a local resonator using topology optimization to tailor bandgaps in plate structures," *Mater. Des.*, vol. 191, p. 108627, Jun. 2020, doi: 10.1016/j.matdes.2020.108627.

[18] G. Yi, Y. C. Shin, H. Yoon, S.-H. Jo, and B. D. Youn, "Topology optimization for phononic band gap maximization considering a target driving frequency," *JMST Adv. 2019 11*, vol. 1, no. 1, pp. 153–159, Jul. 2019, doi:

10.1007/S42791-019-00019-Y.

[19] Z. Liu, H. W. Dong, G. L. Yu, and L. Cheng, “Achieving ultra-broadband and ultra-low-frequency surface wave bandgaps in seismic metamaterials through topology optimization,” *Compos. Struct.*, vol. 295, p. 115863, Sep. 2022, doi: 10.1016/j.compstruct.2022.115863.

[20] Z. Liu, S. B. Shan, H. W. Dong, and L. Cheng, “Topologically customized and surface-mounted meta-devices for Lamb wave manipulation,” *Smart Mater. Struct.*, vol. 31, no. 6, 2022, doi: 10.1088/1361-665X/ac64db.

[21] Z. Liu, H. W. Dong, and G. L. Yu, “Topology optimization of periodic barriers for surface waves,” *Struct. Multidiscip. Optim.*, vol. 63, no. 1, pp. 463–478, 2021, doi: 10.1007/s00158-020-02703-3.

[22] M. Rupin, F. Lemoult, G. Lerosey, and P. Roux, “Experimental demonstration of ordered and disordered multiresonant metamaterials for lamb waves,” *Phys. Rev. Lett.*, vol. 112, no. 23, Jun. 2014, doi: 10.1103/PhysRevLett.112.234301.

[23] E. G. Williams, P. Roux, M. Rupin, and W. A. Kuperman, “Theory of multiresonant metamaterials for A0 Lamb waves,” *Phys. Rev. B - Condens. Matter Mater. Phys.*, vol. 91, no. 10, Mar. 2015, doi: 10.1103/PhysRevB.91.104307.

[24] L. S. S. Pillarisetti, C. J. Lissenden, and P. Shokouhi, “Understanding the role of resonances and anti-resonances in shaping surface-wave bandgaps for metasurfaces,” *J. Appl. Phys.*, vol. 132, no. 16, p. 164901, Oct. 2022, doi: 10.1063/5.0093083.

[25] A. Colombi, P. Roux, S. Guenneau, P. Gueguen, and R. V. Craster, “Forests as a natural seismic metamaterial: Rayleigh wave bandgaps induced by local resonances,” *Sci. Rep.*, vol. 6, 2016, doi: 10.1038/srep19238.

[26] X. Pu, A. Palermo, and A. Marzani, “Lamb’s problem for a half-space coupled to a generic distribution of oscillators at the surface,” *Int. J. Eng. Sci.*, vol. 168, no. March, p. 103547, 2021, doi: 10.1016/j.ijengsci.2021.103547.

[27] D. J. Colquitt, A. Colombi, R. V. Craster, P. Roux, and S. R. L. Guenneau, “Seismic metasurfaces: Sub-wavelength resonators and Rayleigh wave interaction,” *J. Mech. Phys. Solids*, vol. 99, no. December 2016, pp. 379–393, 2017, doi: 10.1016/j.jmps.2016.12.004.

[28] C. J. Lissenden, C. N. Hakoda, and P. Shokouhi, “Control of low-frequency Lamb wave propagation in plates by boundary condition manipulation,” 2021. doi: 10.1063/5.0042576.

[29] C. Hakoda, C. J. Lissenden, and P. Shokouhi, “Clamping resonators for low-frequency S0 Lamb wave reflection,” *Appl. Sci.*, vol. 9, no. 2, 2019, doi: 10.3390/app9020257.

[30] D. Giraldo Guzman, L. S. S. Pillarisetti, S. Sridhar, C. J. Lissenden, M. Frecker, and P. Shokouhi, “Design of resonant elastodynamic metasurfaces to control S0 Lamb waves using topology optimization,” *JASA Express Lett.*, vol. 2, no. 11, p. 115601, Nov. 2022, doi: 10.1121/10.0015123.

[31] D. Giraldo Guzman, L. S. S. Pillarisetti, M. Frecker, C. J. Lissenden, and P. Shokouhi, “Surface wave propagation control with locally resonant metasurfaces using topology-optimized resonators,” *J. Acoust. Soc. Am.*, vol. 155, no. 5, pp. 3172–3182, 2024, doi: 10.1121/10.0025989.

[32] L. B. Beardslee, M. C. Remillieux, and T. J. Ulrich, “Determining material properties of components with complex shapes using Resonant Ultrasound Spectroscopy,” *Appl. Acoust.*, vol. 178, p. 108014, 2021, doi: 10.1016/j.apacoust.2021.108014.

[33] D. Giraldo Guzman, C. Lissenden, P. Shokouhi, and M. Frecker, “Topology Optimization Design of Resonant Structures Based on Antiresonance Eigenfrequency Matching Informed by Harmonic Analysis,” *J. Mech. Des.*, vol. 145, no. 10, Oct. 2023, doi: 10.1115/1.4062882.

[34] P. B. Silva, M. J. Leamy, M. G. D. Geers, and V. G. Kouznetsova, “Emergent subharmonic band gaps in nonlinear locally resonant metamaterials induced by autoparametric resonance,” *Phys. Rev. E*, vol. 99, no. 6, Jun. 2019, doi: 10.1103/PhysRevE.99.063003.

[35] O. M. Silva, M. M. Neves, and A. Lenzi, “On the use of active and reactive input power in topology optimization of one-material structures considering steady-state forced vibration problems,” *J. Sound Vib.*, vol. 464, p. 114989, 2020, doi: 10.1016/j.jsv.2019.114989.

[36] T. Zegard and G. H. Paulino, “Bridging topology optimization and additive manufacturing,” *Struct. Multidiscip. Optim.*, vol. 53, no. 1, pp. 175–192, 2016, doi: 10.1007/s00158-015-1274-4.

[37] J. L. Rose, *Ultrasonic guided waves in solid media*, vol. 9781107048. 2014.

[38] C. Hakoda, C. Lissenden, and J. L. Rose, “Weak form implementation of the semi-analytical finite element (SAFE) method for a variety of elastodynamic waveguides,” *AIP Conf. Proc.*, vol. 1949, 2018, doi: 10.1063/1.5031648.

[39] C. Hakoda, J. Rose, P. Shokouhi, and C. Lissenden, “Using Floquet periodicity to easily calculate dispersion curves and wave structures of homogeneous waveguides,” *AIP Conf. Proc.*, vol. 1949, no. April, 2018, doi: 10.1063/1.5031513.